

# Theory of Geometric Super-resolution for Haptic Sensor Design

Huanbo Sun and Georg Martius Autonomous Learning Group  
 Max Planck Institute for Intelligent Systems  
 Tübingen, 72076, Germany  
 Email: huanbo.sun|georg.martius@tuebingen.mpg.de

Haptic feedback is important to make robots more dexterous and effective. High-resolution haptic sensors are still not widely available, and their application is often bound by robustness issues. A route towards high-resolution and robust sensors is to embed a few sensor units (taxels) into a flexible surface material and use signal processing to achieve sensing with super-resolution accuracy. We propose a theory for geometric super-resolution to guide the development of haptic sensors of this kind. This theory is based on sensor isolines and allows us to predict force sensitivity and accuracy in force magnitude and contact position as a spatial quantity. We evaluate the influence of different factors, such as the elastic properties of the material, using finite element simulations. We compare three representative real sensor unit types, empirically determine their isolines, and validate the theory in a custom-built sensor. Using machine learning techniques, we obtain an average super-resolution factor of 300. As we illustrate, our theory can guide future haptic sensor designs and inform various design choices.

## 1. INTRODUCTION

Haptic sensors are indispensable in robotic applications to enable robots perceiving when, where, and how their bodies are contacting other things [1, 2, 3, 4, 5, 6]. A common theme for surface haptic sensors is to integrate many small sensing units forming a type of grid along a flat or curved surface. Each sensing unit, named taxel, is responsible for sensing interactions near its location. For typical applications, a resolution is desirable that would imply a large number of taxels [4, 5, 7, 8, 9, 10, 11]. This is true both for small surface sensing, e.g. at the fingertips and for large surfaces, e.g. around limbs. Technical challenges arise concerning the physical size of the taxels as well as growing manufacturing and wiring costs [12].

Naturally, efforts have been made to reduce the number of taxels [13, 14, 15, 16, 17, 18, 19, 20, 21]. The reduction is generally enabled by the fact that a taxel can monitor not only a tiny area but an extended patch on the surface and that we are interested in a subset of all possible stimulation patterns, for instance, a few touch-points. The particular material properties lead to a characteristic spread of contact information to the sensing taxels. Different physical effects can be used, such as electrical resistance [14, 15], magnetic flux [16], thermo- and fluid-dynamics [18], geometric and mechanical properties [19, 20, 21], and so forth. The central idea is to solve the inverse problem of inferring haptic information from a few sensors, effectively creating high-resolution virtual taxels. This is also referred to as super-resolution sensing [22].

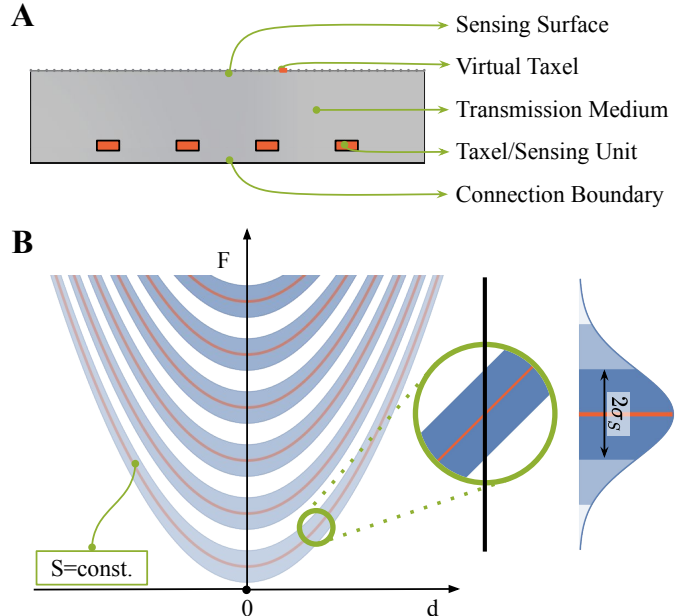


Fig. 1. Introduction of the model. A: 1D sensor layout with sparsely placed real taxels and highly resolved virtual taxels. B: The taxel isolines (orange) are the force  $F$  needed to elicit the same taxel-value  $S$  depending on the distance  $d$  from the sensor unit. Measurement noise is shown in shaded blue.

How much “super-resolution” can we obtain? What is the expected sensitivity of the sensing system? Which surface material and which sensor is suitable? This paper aims to provide answers to these questions from a theoretical perspective as well as from a practical point of view by applying the method to three common sensor types and evaluating a custom-built sensor design. We introduce a theory that allows us to predict spatially resolved properties, such as accuracy and sensitivity for single and double contact, based on a single characteristic of the material-taxel interplay: taxel value isolines.

The model we use is a sensor comprising discrete taxels sparsely distributed in a continuous transmission medium underneath a sensing surface as shown in Fig. 1(A). For sensing devices that can be described by this model, we

- derive the single contact accuracy for position and force magnitude inference based on the taxel isolines;
- determine the minimal force profile for which localization is possible;
- provide conditions for simultaneous contacts to be distinguished;

- evaluate three real sensor types: strain gauge, accelerometer and barometric sensor, and provide their isolines;
- design a 1-dimension (1D) barometer-based sensor with 300-fold super-resolution.

We start with the model description and continue with the analysis in 1-dimension (1D) in Section 3, and generalize the analysis to 2-dimensions (2D) in Section 4. In Section 5, we evaluate different influence factors for the sensor design with help of a finite element method (FEM). The isolines of the three real sensor types molded in soft material are presented in Section 6. We validate the theoretical analysis with a custom-built sensor and present its performance in Section 7.

## 2. THE MODEL

We consider a class of haptic sensing devices intended for measuring force interactions on an extended surface that have an elastic transmission medium covering or embedding physical sensor units (taxels). A one-dimensional model is shown in Fig. 1(A). A single taxel value  $s$  is a function of the applied contact force strength  $F$ , and the displacement  $d$  between the contact center and the taxel center:

$$s = f(F, d) + \epsilon_s, \quad (1)$$

where  $\epsilon_s$  is the taxel measurement noise with standard deviation  $\sigma_s$ :

$$\epsilon_s \sim \mathcal{N}(0, \sigma_s^2). \quad (2)$$

We use a constant  $c$  as a unit transformation function to correlate the sensor value unit ( $\mathcal{U}$ , e.g., Pascal in pressure measurement) with force ( $N$ ) and make them consistent in the equations. Formally, the sensor response to an applied force at distance 0 should be  $f(F, 0) = c \cdot F$  and to simplify the notation we set  $c = 1$ . It has an unit of  $\mathcal{U}/N$  here. However, our analysis can be easily adapted for different values of  $c$  and for nonlinear monotonous relationships.

One of our main contributions is to introduce the *taxel value isolines* as an important characteristic function of the system.

*Definition 1:* Taxel value isolines (TVI) are a family of curves

$$I^S(d) = \begin{cases} F & \text{with } f(F, d) = S \\ \text{undefined} & \text{if no such } F \end{cases} \quad (3)$$

where the mean taxel output (Eq. 1) has a constant value  $S$ .

The TVI for the model system and the effect of measurement noise are shown in Fig. 1(B). Intuitively, the isolines quantify how much force is needed along the surface to yield the same sensor value. To activate a taxel with a particular value, the required force strength is smaller when the contact location is closer to the taxel. Based on these isolines, we can derive the accuracy distributions of contact localization and force quantification, and the distribution of sensitivity over the sensing surface. Our method is based on the conditions for unique nonlinear triangulation and the geometry of intersecting isolines with their uncertainty bands.

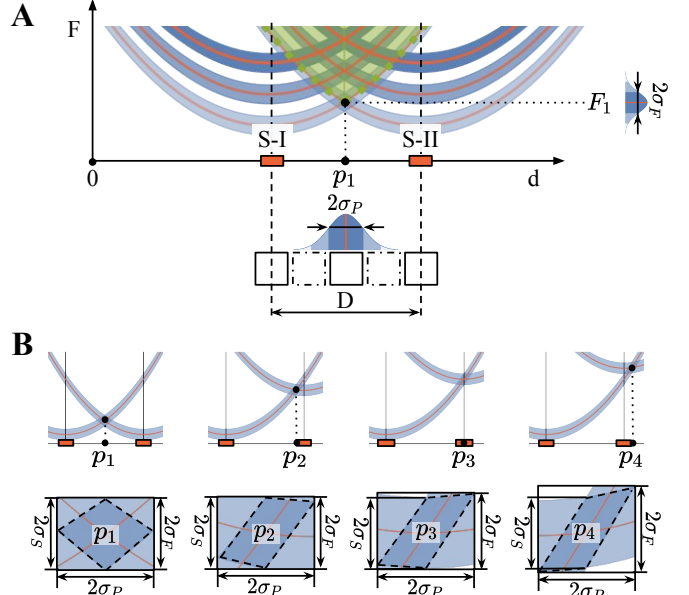


Fig. 2. Model for contact point localization at super-resolution. **A:** The intersection of TVIs of two sensors (marked by S-I and S-II). The place where the lines corresponding to the particular sensor readings cross is the contact location. A hypothetical point is marked as  $p_1$ . The measurement noise leads to uncertainty of the position  $\sigma_p$  and force  $\sigma_F$ . **B:** Different intersection types.

## 3. SUPER-RESOLUTION IN 1D

When can a single contact point be localized at super-resolution, meaning much more accurate than the distance between taxels? Intuitively, this is possible when two or more taxels measure nonzero responses to the contact force and the activation pattern of the taxels is unique for this location. More formally, this condition can be analyzed with the TVIs. The minimal setting of two taxels located at a distance of  $D$  is shown in Fig. 2.

A particular contact event causes a sensor reading in both sensors  $S_1$  and  $S_2$ . The TVI corresponding to a sensor reading of  $S_1$  relates the position to the force of the potential contact point. Only if the TVIs from both sensors intersect, the contact position can be localized, up to some uncertainty introduced by the measurement noise  $\sigma_s$  (Eq. 1). With this insight, we can derive the minimal force sensitivity  $F_S$  that allows for super-resolution localization, i.e. where at least two isolines intersect. We can find this minimal force, where the isolines corresponding to the smallest taxel sensitivity  $S_{\min}$  intersects with TVIs from neighboring taxels. The area where  $F \geq F_S$  is shaded in green in Fig. 2(A).

As we assume an additive measurement noise, the uncertainty is also added to the isolines as shown in Fig. 2(A). What does this mean for the ability to localize the contact position and to infer force magnitude? For the case of parabolic TVIs, we have to consider different possible scenarios as shown in Fig. 2(B). For contact locations between the two taxels, marked with  $p_1, p_2$  in Fig. 2(B), the standard deviation for the force estimation is actually constant and given by  $\sigma_s$ . There is no dependency on the taxel distance  $D$ . For contact points close to the taxel and outside the taxel pair, the uncertainty of the force magnitude grows with distance ( $p_3, p_4$  in Fig. 2(B)). The standard deviation for position localization  $\sigma_p$  is typically

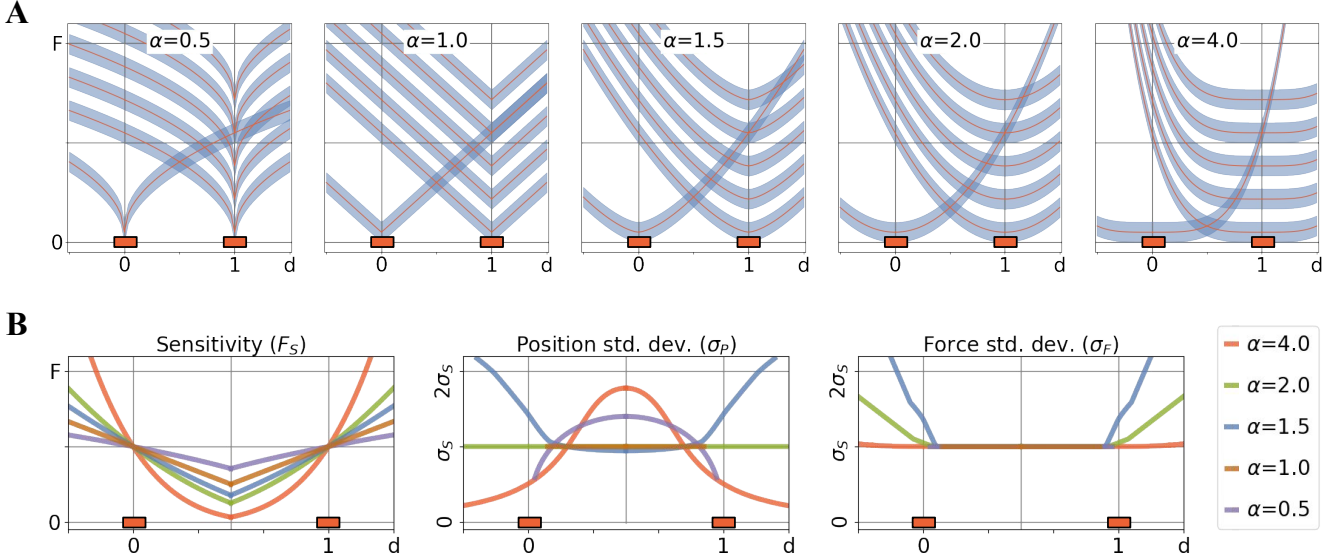


Fig. 3. Effect of TVIs shape on super-resolution characteristics. **A:** TVIs for two taxels (at distance 1) with different attenuation exponents  $\alpha$ . Note the different shapes of the intersection areas. **B:** Resulting sensitivity, standard deviation of position localization and standard deviation of force inference. For  $\alpha < 1$  has no unique solution, but is still provided for reference. More details are in the main text.

largest in the center between the taxels and gets smaller on either side, except for  $1 \leq \alpha \leq 2$ . The exact equations to compute these standard deviations are given in Appendix B and a visualization is given below.

Knowing the position accuracy  $\sigma_P$ , we can quantify the super-resolution capabilities. For simplicity, we use  $2\sigma_P$  as the size of a virtual taxel, as shown in Fig. 2(A), corresponding to a confidence interval of about 68%. Thus, the spatial resolution is  $2\sigma_P$  and between two sensors at a distance  $D$  we can distinguish  $D/2\sigma_P$  virtual taxels, which we define as *super-resolution factor*:

$$\Omega = \frac{D}{2\sigma_P} \quad (4)$$

### 3.1. Influence of the Isoline Shape

The shape of the TVIs depends on the properties of the transition medium and the sensor unit type. We study the impact of the TVI shape on the accuracy of single contact force inference. We follow the general model that the response of a taxel to a force on the surface decreases monotonously with distance from the taxel center. This in turn leads to a monotonously increasing TVI. We assume the attenuation of taxel response behaves as  $s \propto 1/|d|^\alpha$  for a force at distance  $|d|$  from the taxel center with the attenuation exponent  $\alpha$ . Without loss of generality, we consider two taxels at a distance of 1. Their TVIs are given by

$$I_1^S(d) = g(S) + |d|^\alpha, \quad (5)$$

$$I_2^S(d, s) = g(S) + |1 - d|^\alpha. \quad (6)$$

where  $g(S)$  is force corresponding to the measurement at distance 0. The TVIs for different attenuation behaviors are shown in Fig. 3(A). Already the visual inspection of the TVI intersection areas reveals that the accuracy of super-resolution sensing will be strongly effected by  $\alpha$ . For instance,

for linear attenuation ( $\alpha = 1$ ), the localization will only be possible between the taxels, but not outside (unbounded intersection area). For concave curves ( $\alpha < 1$ ), there can be three intersection areas: one is between the two taxels and the other two are outside, which makes the reconstruction not unique. For the sake of comparison, we assume that in this case the correct intersection is known.

Smaller attenuation exponent  $\alpha$  yields a smaller sensitivity (bigger  $F_S$ ) between the taxels but in general a more homogeneous distribution (Fig. 3(B)). The position accuracy, measured by the standard deviation  $\sigma_P$  is constant for  $\alpha = 2$ . For normalized TVIs, as used here for comparison,  $\sigma_P = \sigma_S$ . The general case is given below. For  $\alpha > 2$  and  $\alpha < 1$  we find a reduced position accuracy between the taxels. Interestingly, for  $\alpha > 2$ , the reduced position error at the outside is paid by a reduced force sensitivity. For  $1 < \alpha < 2$ , the position error and force error are both high outside which should be avoided in sensor design. The ability to infer the force magnitude, given by  $\sigma_F$  is constant between the two taxels, irrespective of  $\alpha$ . For contact points outside, larger values of  $\alpha$  are better whereas for  $\alpha \leq 1$  no detection is possible.

From this analysis,  $\alpha = 2$  yields the best overall characteristics, namely having high force sensitivity (small  $F_S$ ), high position and force accuracy (small  $\sigma_P, \sigma_F$  respectively). Values  $\alpha > 2$  trade off some super-resolution by sensitivity but are generally also good. Taxel response attenuation with exponent  $\alpha < 2$  should be avoided, if possible.

An approximate relationship between  $\sigma_P$  and  $\sigma_S$  for the more general TVIs  $I^S(d) = g(S) + \lambda|d|^\alpha$  is given by:

$$\sigma_P = \frac{2\sigma_S}{m_1 + m_2} \quad (7)$$

where  $m_1 = \lambda\alpha|d|^{\alpha-1}$  and  $m_2 = \lambda\alpha|d - D|^{\alpha-1}$  are the absolute derivatives of the TVIs as detailed in Appendix A. Using the position accuracy at  $d = D/2$  (which is the worst for typical exponents  $\alpha \geq 2$ ) we can compute the super-resolution

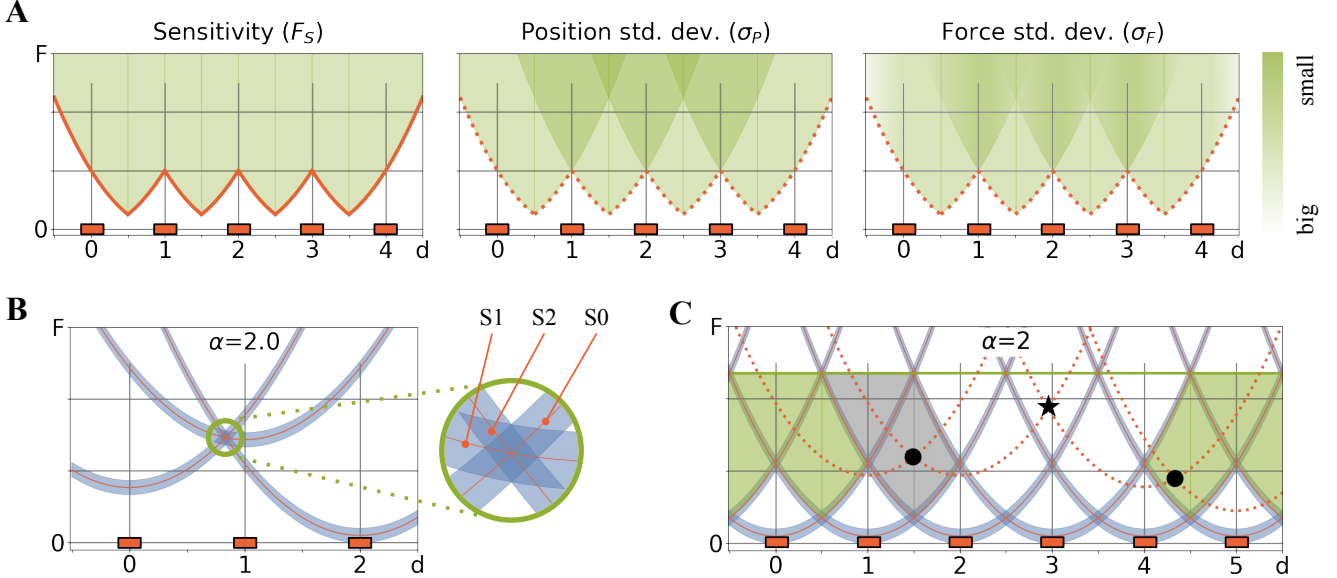


Fig. 4. Theoretical super-resolution characteristics of a 1D sensor with 5 taxels (sensors units). **A:** The spatial distribution of sensitivity and accuracy for a single contact. Below the orange line, no super-resolution localization is possible. Notice the increase in accuracy for higher forces because multiple taxels are activated. **B:** Three taxels localizing a single contact. **C:** Six taxels discriminate two simultaneous contacts. For two contacts, each in one of the green shaded area, localization is possible (two-contact sensitivity). If one point is in the gray shaded area, an additional spurious point would be detected (\*).

factor analytically using Eq. (4):

$$\Omega = \frac{D\lambda\alpha|D/2|^{\alpha-1}}{2\sigma_S} \quad (8)$$

### 3.2. Multiple Taxels in a Line

A real sensor should clearly contain more than 2 taxels, so let us consider multiple taxels (with quadratic isolines) equidistantly placed in the transmission medium (as shown in Fig. 1. The sensitivity  $F_S$  (see Fig. 2(A)) is shown in Fig. 4(A) together with the accuracy of localization  $\sigma_P$  and force quantification  $\sigma_F$ . The sensitivity is not homogeneous and is higher between taxels, which might be a surprising result at first glance. As expected, in the area where more than two taxels respond to the contact stimulation, a higher localization accuracy is possible, as shown in Fig. 4(B). The intersection area is smaller and due to averaging independent noise measurements, the variance also reduces with the number of TVIs intersecting. This also explains the reduction in uncertainty about the contact force. In summary, the most important take-home message is to have multiple taxels responding to a contact force because it improves the accuracy. Closer placement of taxels increases both sensitivity and accuracy and reducing taxel measurement noise improves accuracy but not the sensitivity.

### 3.3. Multiple contact points

In many applications, we are interested in detecting multiple simultaneous contact points. To detect two points, we need at first glance 2 pairs of taxels. However, when the contact points are too close, spurious contact points would be detected due to additional intersections of TVIs. The basic condition for successfully distinguishing them is shown in Fig. 4(C) and marked by a green shaded area. Within the maximal force

range, no TVI from a taxel evoked by one contact should intersect with a TVI from a taxel stimulated by the other contact. Thus, the minimum distance depends on the width of the TVIs and the maximal force. The figure shows the problem of spurious intersection points. Setting the green force threshold, only one additional spurious point would be detected (\*) when one of two contacts is in the shaded gray area. With higher force threshold, more spurious point are included.

## 4. SUPER-RESOLUTION IN 2D

The above analysis for the 1-dimensional case helps us to investigate a sensor with a flat or curved 2-dimensional sensing surface. To simplify the analysis, we continue to assume a homogeneous transmission medium and an isotropic sensor unit, which is, for instance, approximately true for barometric sensors but violated for strain-gauge sensors.

We first consider a flat 2D sensing surface with coordinates  $x$  and  $y$ . The concept of isolines translates into isosurfaces, as shown in Fig. 5(A). However, we still call them TVIs for consistency. Clearly, with only two taxels, an accurate localization can only be done along one dimension, but not along two. The intersection volume of the TVIs is presented in Fig. 5(B). For attenuation exponents  $\alpha \neq 2$  the intersection volume changes depending on the transversal position  $y$  as shown in Fig. 5(C).

To make proper super-resolution localization possible, at least 3 taxels need to respond to a stimulus, as shown in Fig. 5(D-I). As before, the accuracy is increased if more taxels are involved, as shown in Fig. 5(D-II) for 4 taxels arranged in a regular grid. We also compute the sensitivity distribution over the sensing surface for both sensor arrangements. The honeycomb pattern allows for a more homogeneous sensitivity.

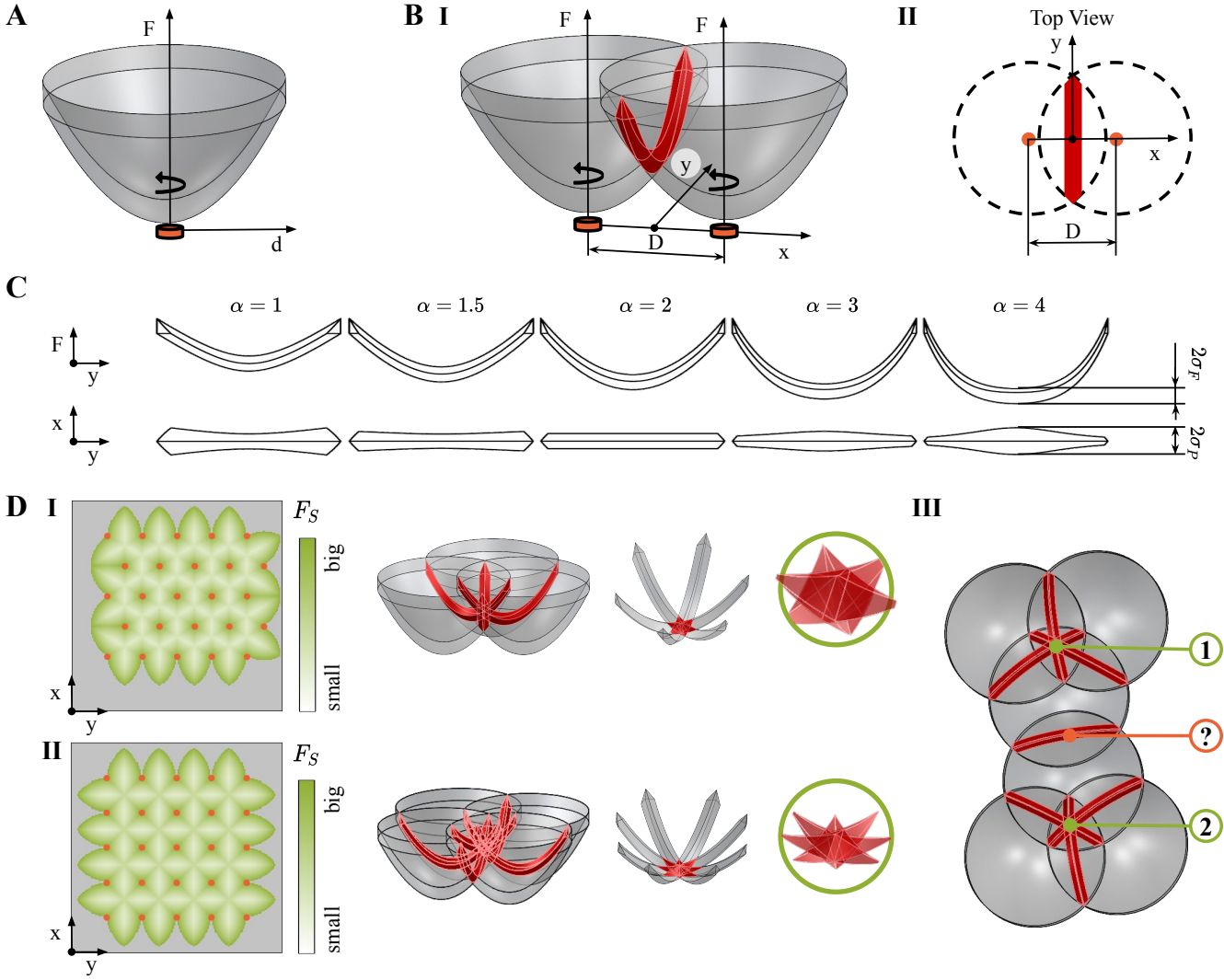


Fig. 5. Taxel values isolines for a 2D sensing surface. **A**: Taxel value isoline (iso-surface) for a single taxel. **B**: Intersection volume (due to measurement uncertainty) for two taxels at a distance  $D$  along the  $x$  axis, see top view. The localization would be very uncertain along the  $y$  direction. **C**: Intersection volume for different attenuation exponents  $\alpha$ . **D**: Proper localization requires at least 3 taxels for 1 contact point. **I** shows a hexagonal sensor placement with resulting sensitivity over the surface and an illustration of the intersection volume of the TVIs from 3 taxels. **II** is the same for a grid and 4 taxels. **III** illustrates a spurious contact localization for 2 contact points and 6 taxels (marked with "?"), however its uncertainty would be very large.

To detect two simultaneous contacts, at least 6 taxels are required to respond. Similar to the 1D case, if the contact points are too close, spurious intersections can occur. In some cases, as shown in Fig. 5(D-III), spurious intersections can be ruled out because of high elongation in one direction. This is a new feature that was not observed in 1D.

Very similar considerations are also valid for curved sensing surfaces, which is illustrated in Fig. 11 in Appendix C.

## 5. PHYSICAL FACTORS INFLUENCING TVIs

Let us investigate the influences of transition medium (e.g. elastomer) properties and taxel placement on the TVIs and on the sensitivity. External contact at the sensing surface causes deformation of the transmission medium that can be measured by physical sensor units (taxels). In this section, we assume the taxels are able to measure deformation/strain within the medium, either isotropically or directionally.

In principle, the deformation can be described by the absolute movement of elements, called displacement, and by the relative movement of elements, denoted as strain. To study the isolines we consider the displacement as a measure of deformation. The displacement is computed for a static mechanical model simulated with the finite element method (FEM) using Ansys [23]. The questions we want to answer in this section are: Where to place the sensor units within the transition medium? How thick should be the transition medium? What is the effect of material properties such as the Poisson's ratio?

### 5.1. Simulation model

The full model is a cylinder-shaped sensor transmission medium with a diameter of 200 mm and a thickness of 5 mm, 10 mm or 15 mm, but we simplify the model in the FEM simulation into a 2D plane due to the axis-symmetric property of the cylinder and the spherical indenter (10 mm diameter) as

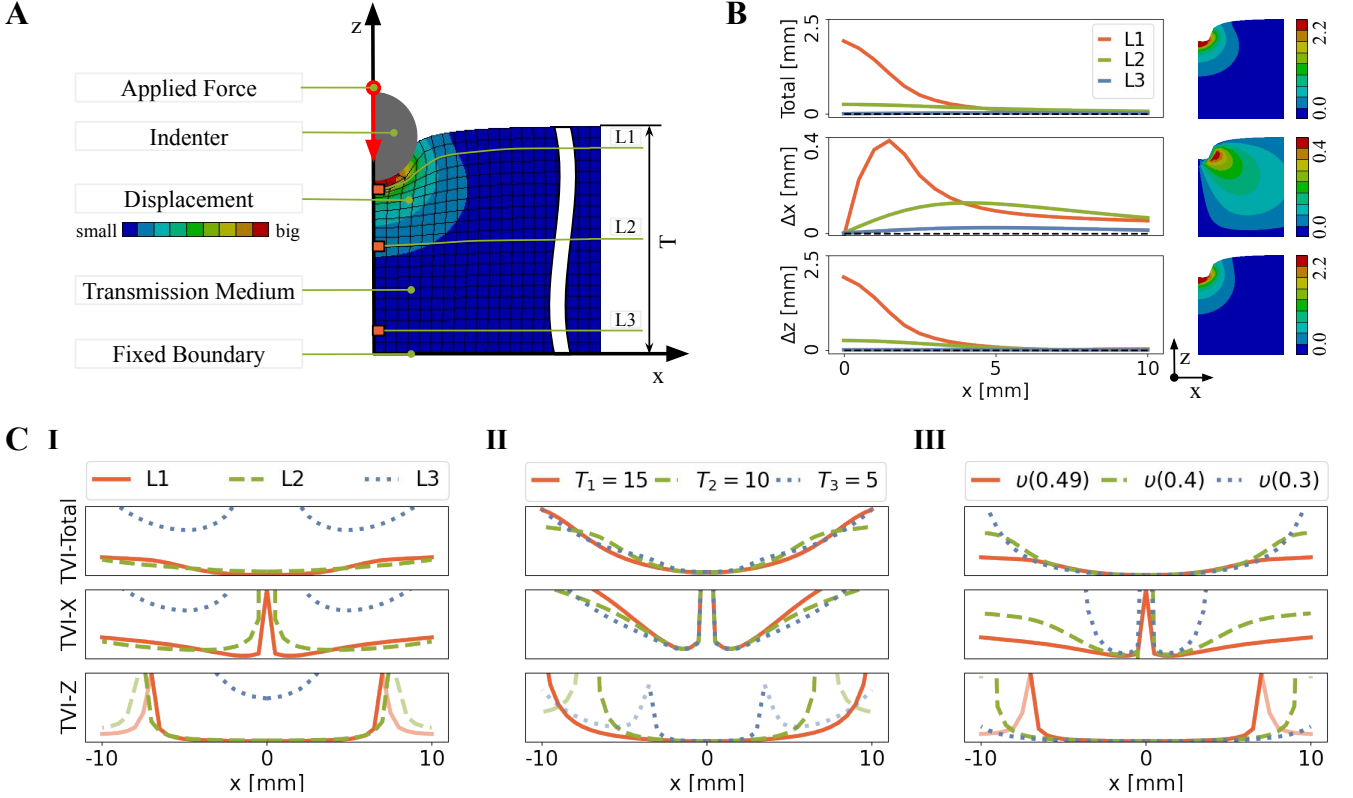


Fig. 6. FEM model to study different design choices. A: The model: because of symmetry, only one half is shown. The thickness is  $T = 10$  mm and we consider taxels at level  $L1 = T - 1$  mm,  $L2 = T - 5$  mm and  $L3 = T - 9$  mm. B: Total displacement maps as well as its  $x$ - and  $z$ -components. C: TVIs for hypothetical sensors measuring total displacement or component-wise displacement, for different taxel depth (I), material thickness (II), and Poisson's ratios (III). TVIs for negative sensor values are in a light shade. Default configuration is  $\nu = 0.49$  and  $L1 = T - 1$  mm.

shown in Fig. 6(A). The transition medium is constrained at the bottom by a fixed boundary. We analyse the displacement when a normal force is applied to the contact surface via the indenter. In Fig. 6(B) the displacement is evaluated in  $x$ - and  $z$ -direction, as well as in terms of total displacement. Considering the displacement at three different depths, close to the sensing surface (L1), in the middle (L2), and close to the fixed boundary (L3), shows significant differences. The displacement in depth direction ( $\Delta z$ ) decreases monotonously with distance, but is much stronger at L1 than at L3. The radial displacement ( $\Delta x$ ) first increases and then attenuates, which will give rise to non-monotonous TVIs.

## 5.2. Taxel Depth

The dependency of the deformation on the depth has an impact on the TVIs. Figure 6(C-I) shows the TVIs for ideal displacement sensors at three different depths (L1-L3) described above. We plot the TVI for the smallest non-zero taxel value. However, because there can also be negative displacements, we add a light-shaded TVI for small negative values if occurring. When measuring depth deformation, the TVIs have a convex shape for positive sensor values and a second parabola at either side for the negative sensor values. This holds for all depths, although only visible for L1 due to a limited plot range. The radial direction is more surprising, as the center is not moving radially, the TVIs have a pole in the center. The total deformation is monotonous for low to middle taxel depths

(L1 and L2). Depending on the physical quantity measured by the real sensor unit, this leads to different conclusions: For strain gauges and accelerometers, for instance, the global displacement can be considered as a good proxy, as they measure the curvature and inclination of the material. Thus, these sensors should be more close to the sensing surface. Barometric sensors, for instance, measure local displacement, for which we cannot give a recommendation at this point.

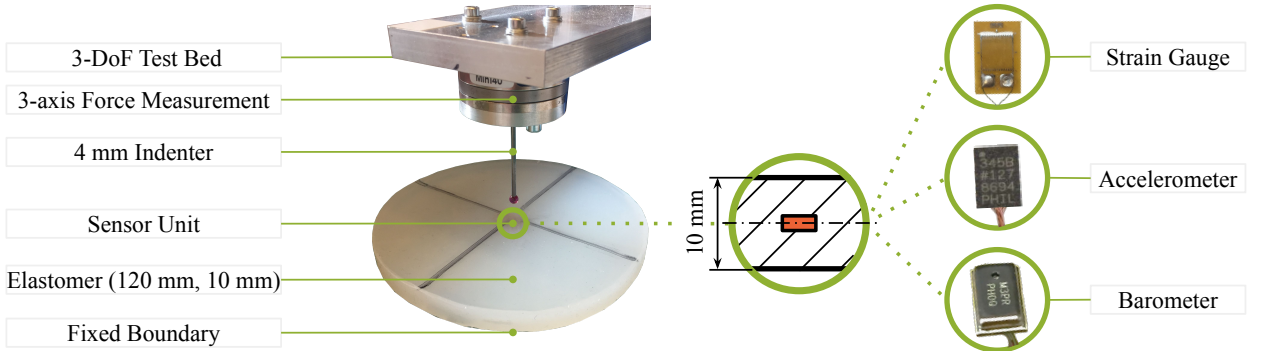
## 5.3. Sensing Surface Thickness

Guided by the previous result, we consider a taxel at depth L1 (1 mm below the sensing surface) for different total thicknesses of the elastomer. Figure 6(C-II) presents the TVIs. The radial deformation is, as expected, only a little effected by the amount of material underneath the taxel. The depth deformation, on the other hand, shows a much larger effect of thickness, because for smaller thickness we get less displacement. In summary, the thicker material causes more displacement and in turn increases the sensitivity, because the fixed boundary becomes less dominant.

## 5.4. Material Properties

The main two properties of the transmission material we consider are the Young's modulus and the Poisson's ratio. The Young's modulus describes how easy the material deforms and has a proportional impact on the deformation. A soft material (small Young's modulus) improves sensitivity, but

A



B

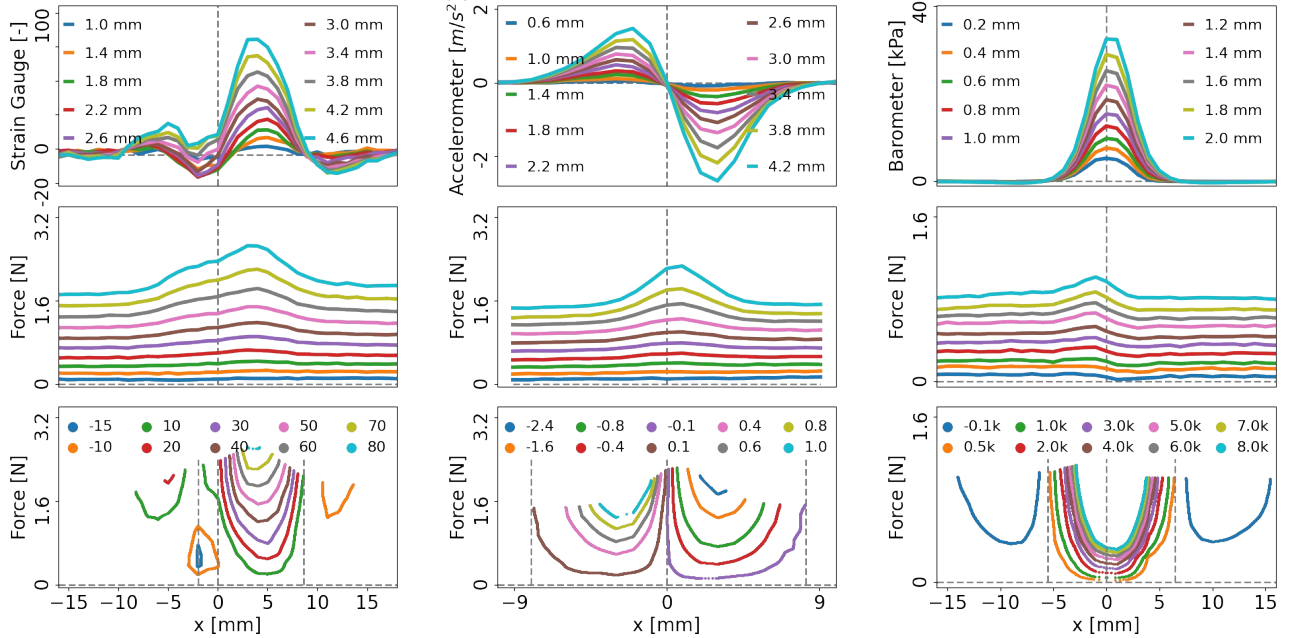


Fig. 7. Response and TVIs of real sensor units. **A:** The experimental setup. The black lines on the disc mark the stimulation points. **B:** Sensor response (top), true indentation force (middle), and TVIs (bottom) for strain gauge (left), accelerometer (center), and barometer (right). Lines are presented for different penetration depths of the indenter and different sensor values in the bottom row. Barometers have TVIs that are most similar to our theoretical model.

is also increasingly deformed by inertial effects. Poisson's ratio measures the relative transversal/radial expansion when the material is axially compressed. Most elastomers have Poisson's ratio around 0.5 and metals have around 0.3 [24]. Figure 6(C-III) shows the TVIs for different Poisson's ratios. Decreasing the ratio, the radial displacement becomes much less sensitive, whereas the depth displacement has higher sensitivity (lower TVIs). Thus, depending on the measurement direction of the real sensor unit, different Poisson's ratios are preferred.

## 6. TAXEL VALUE ISOLINES OF REAL SENSORS

We augment our theoretical analysis by measuring the response curves of three suitable sensors. We consider strain gauges that measure the change in curvature along one direction averaged over the sensing area [20, 21]; accelerometers that are able to measure the absolute inclination of the local elastomer patch using the gravity direction as a reference [25]; and barometers that sense the volume change

caused by the material's deformation in the form of isotropic pressure [26, 27].

Our experimental setup (Fig. 7(A)) is as follows: we mold a single sensor unit at the center of an elastomer disc (120 mm diameter and 4 mm) and measure the sensor unit's response when indenting it with a controlled depth along two perpendicular axes using an automated 3-DoF test bed with a force sensor (for details see Appendix E).

Based on the recorded data, we present in Fig. 7(B) the sensor values, the applied forces, and the TVIs for each sensor type as a spatially changing quantity. We only show the data for one of the two directions. For the strain gauge unit this is along its measurement direction. The barometer is fairly isotropic up to small deviations because of the rectangular sensor housing. Accelerometers are interesting, because they can distinguish between both directions.

We mainly focus the discussion on the presented TVIs and refer to Appendix E for more detail. The strain gauge has a non-monotonic behavior where one strain gauge value has several position-force possibilities. The accelerometer does

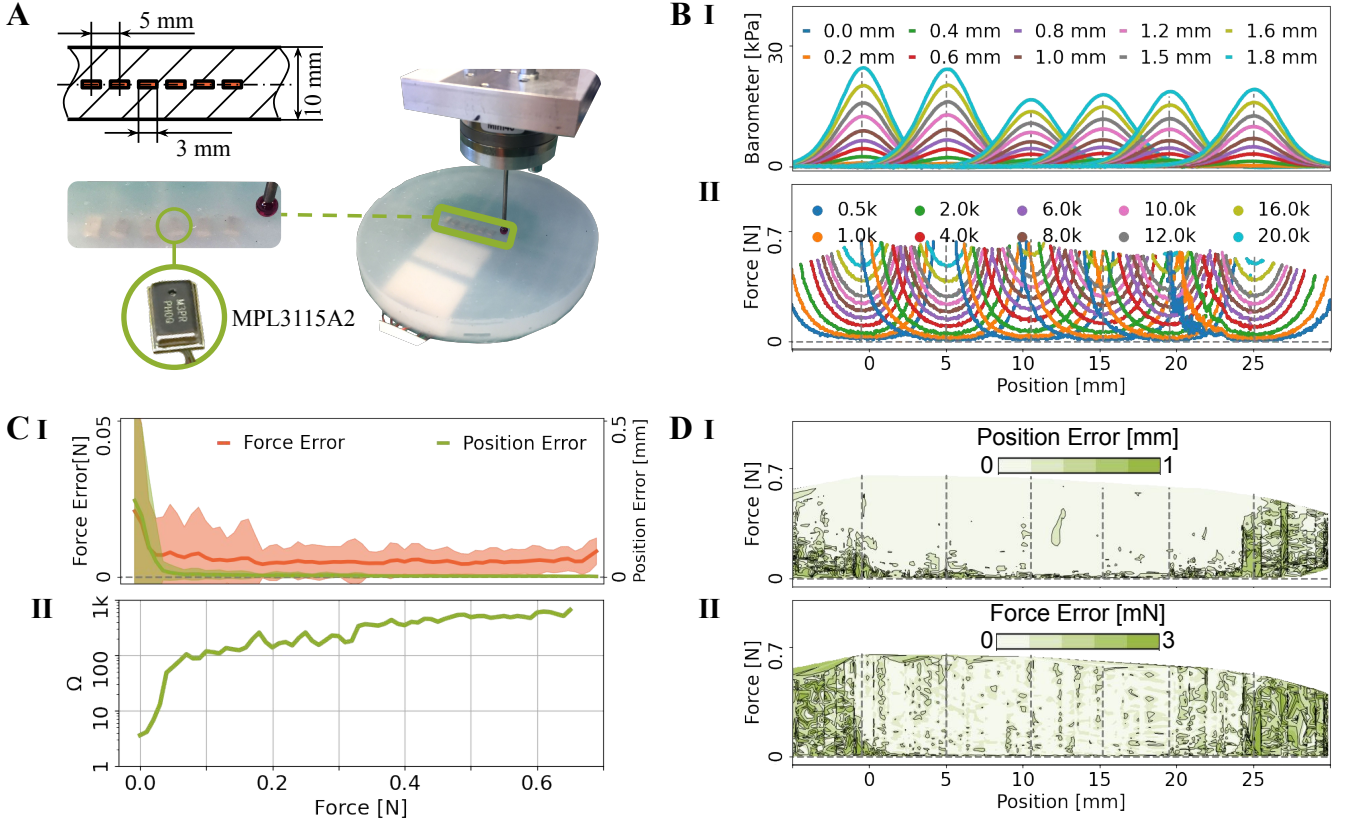


Fig. 8. Real line-sensor device with 6 barometer taxels at a distance of 5mm. **A:** Sensor device with stimulation test bed; **B:** Taxel response for different indentation depths (**I**) and resulting TVIs (**II**); **C,D:** Quantitative evaluation of the sensor device using a machine learning model to infer the position and force magnitude; **C-I** Position and force error depending on stimulation force: mean and std. dev over the 25 mm between taxel 1 and 6. **C-II** Superresolution factor depending on the contact force magnitude; **D** Spatially resolved position error (**I**) and force error (**II**), c.f. Fig. 4(A).

not have this problem, however, it has a “blind spot” directly above the sensor unit (no inclination), however, this is a tiny area. Note that the TVIs on both sides are for different sensor values, so super-resolution localization is well possible. We leave a theoretical analysis of these TVI shapes for future work. The barometer shows the convex and monotonic properties as described in our proposed theory. Notice the two blue “wings” which are the TVI for negative values caused by the lateral pulling force from distant contacts.

## 7. EXPERIMENTAL VALIDATION

Due to the convexity and symmetry of the barometer’s isolines, we use it to validate our proposed theory. We mold six barometers in the elastomer along a straight line with approximately 5 mm distance to each other as shown in Fig. 8A. The test bed carries a 4 mm spherical indenter and contacts the surface along the sensor placement center line. Sensor values, force values, and indentation positions and depths are recorded at 1000 positions evenly along the line (40 mm in total) with 40 incremental indentation depths (0.05 mm each) at each position. The resulting taxel responses and the TVIs are presented in Fig. 8B. They suggest a very good super-resolution potential.

Our proposed theory formulates a fundamental basis for inferring contact information in terms of variance prediction:  $\sigma_P$  and  $\sigma_F$ . The inference of variances is equivalent to solve

the problem of minimizing the least squares in the data-driven regression setting. Thus, we employ two machine learning models to predict the indentation position and force magnitude, respectively, and set a L2 loss (least squares) as the loss function for both. For the architecture and training details, see Appendix F.1. The results are summarized in Fig. 8(C & D). The inference accuracy of the position and force magnitude is higher with stronger indentation force, but generally very accurate (measured at locations that were not included during training). Figure 8(C-II) shows the averaged super-resolution factor  $\Omega$  (Eq. 4), i. e., the number of virtual taxels between two adjunct barometers. The position accuracy  $\sigma_P$  is calculated as the mean plus standard deviation of the position error. Higher force allows for higher super-resolution. Averaging it over the applied force range (from 2 mN to 0.7 N), we obtain an average super-resolution factor of 300.

The spatial resolution of position error and force magnitude error of the prediction model is shown in Fig. 8D. The overall shape resembles our theoretical prediction, c.f. Fig. 4A.

## 8. DISCUSSION

We present a new way to characterize, analyze, and predict force sensation at super-resolution for haptic sensors. Our theory is based on sensor isolines that allow for a direct assessment of the uniqueness of contact position reconstruction. We derive quantities like minimal sensitivity, localization,

and force sensing accuracy. This allows us to analytically compute the super-resolution factor, namely, the number of distinguishable locations between two real sensor units.

With the help of an FEM model, we give guidelines for common design choices, such as placement of the sensor units within an elastomer as well as material properties. We analyze three commonly used sensor types: strain gauges, accelerometers, and barometers. Both accelerometers as well as barometers show the necessary properties for super-resolution sensation. We conduct a small case study to evaluate our theory using a line of barometer sensor units. Following our theoretically derived design choices enables us to achieve a remarkable performance of 300 fold super-resolution with a position accuracy of 1/60 mm.

We hope that our approach can help the design of capable haptic sensors. A few take-home messages can be summarized as follows: The sensor units in the transmission medium (elastomer) should have convex isolines. It is beneficial to have the sensor units “float” in the center of the elastomer or closer to the sensing surface. A flexible wiring helps to have best sensitivity. A thicker elastomer layer seems beneficial, and materials with small Young’s modulus, high Poisson’s ratio, and big yield strength are recommended. The distance between sensor units should be such that for a majority of forces the isolines of neighboring taxels intersect. For inferring simultaneous contacts, however, a limited receptive field of the units reduces spurious detections.

Future work will be devoted to analyze the accelerometers in more detail and investigate shear forces. Furthermore, structured transmission media e.g. with ridges [28] and with multiple layers [29] are an interesting direction.

#### ACKNOWLEDGMENTS

**Funding:** The authors thank the China Scholarship Council (CSC) and the International Max Planck Research School for Intelligent Systems (IMPRS-IS) for supporting H.S. G.M. is member of the Machine Learning Cluster of Excellence, funded by the Deutsche Forschungsgemeinschaft (DFG, German Research Foundation) under Germany’s Excellence Strategy – EXC number 2064/1 – Project number 390727645. We acknowledge the support from the German Federal Ministry of Education and Research (BMBF) through the Tübingen AI Center (FKZ: 01IS18039B). **Author contributions:** H.S. and G.M. conceived the method and the experiments, drafted the manuscript and revised it. H.S. designed and constructed the hardware, developed fabrication methods, designed and conducted experiments, collected and analyzed the data. G.M. supervised the data analysis. We thank Anna Levina for discussions on the analytic solution for  $\sigma_P$ . **Competing interests:** There is no competing interests involved. **Data and materials availability:** The data that support the findings of this study are available from either corresponding author, H.S. or G.M., upon request.

#### REFERENCES

- [1] J. C. Yang, J. Mun, S. Y. Kwon, S. Park, Z. Bao, and S. Park, “Electronic Skin: Recent Progress and Future Prospects for Skin-Attachable Devices for Health Monitoring, Robotics, and Prosthetics,” *Advanced Materials*, vol. 31, no. 48, p. 1904765, 2019.
- [2] Q. Li, O. Kroemer, Z. Su, F. F. Veiga, M. Kaboli, and H. J. Ritter, “A Review of Tactile Information: Perception and Action Through Touch,” *IEEE Transactions on Robotics*, vol. 36, no. 6, pp. 1619–1634, 2020.
- [3] M. L. Hammock, A. Chortos, B. C.-K. Tee, J. B.-H. Tok, and Z. Bao, “25th Anniversary Article: The Evolution of Electronic Skin (E-Skin): A Brief History, Design Considerations, and Recent Progress,” *Advanced Materials*, vol. 25, no. 42, pp. 5997–6038, 2013.
- [4] R. S. Dahiya, G. Metta, M. Valle, and G. Sandini, “Tactile Sensing—From Humans to Humanoids,” *IEEE Transactions on Robotics*, vol. 26, no. 1, pp. 1–20, 2010.
- [5] K. Chin, T. Hellebrekers, and C. Majidi, “Machine Learning for Soft Robotic Sensing and Control,” *Advanced Intelligent Systems*, vol. 2, no. 6, p. 1900171, 2020.
- [6] Z. Kappassov, J.-A. Corrales, and V. Perdereau, “Tactile sensing in dexterous robot hands — Review,” *Robotics and Autonomous Systems*, vol. 74, pp. 195–220, 2015.
- [7] M. T. Francomano, D. Accoto, and E. Guglielmelli, “Artificial Sense of Slip—A Review,” *IEEE Sensors Journal*, vol. 13, no. 7, pp. 2489–2498, 2013.
- [8] R. S. Dahiya, P. Mittendorfer, M. Valle, G. Cheng, and V. J. Lumelsky, “Directions Toward Effective Utilization of Tactile Skin: A Review,” *IEEE Sensors Journal*, vol. 13, no. 11, pp. 4121–4138, 2013.
- [9] R. Balasubramanian and V. J. Santos, *The Human Hand as an Inspiration for Robot Hand Development*. Springer Publishing Company, Incorporated, 2014.
- [10] E. Cheung and V. J. Lumelsky, “Proximity sensing in robot manipulator motion planning: system and implementation issues,” *IEEE Transactions on Robotics and Automation*, vol. 5, no. 6, pp. 740–751, 1989.
- [11] D. Um, B. Stankovic, K. Giles, T. Hammond, and V. Lumelsky, “A modularized sensitive skin for motion planning in uncertain environments,” in *Proceedings of the IEEE International Conference on Robotics and Automation (ICRA)*, vol. 1, 1998, pp. 7–12 vol.1.
- [12] C. Bartolozzi, L. Natale, F. Nori, and G. Metta, “Robots with a sense of touch,” *Nature Materials*, vol. 15, no. 9, pp. 921–925, Sep 2016.
- [13] J. A. Fishel and G. E. Loeb, “Sensing tactile microvibrations with the BioTac — Comparison with human sensitivity,” in *Proceedings of the IEEE International Conference on Biomedical Robotics and Biomechatronics (BioRob)*, 2012, pp. 1122–1127.
- [14] H. Lee, D. Kwon, H. Cho, I. Park, and J. Kim, “Soft Nanocomposite Based Multi-point, Multi-directional Strain Mapping Sensor Using Anisotropic Electrical Impedance Tomography,” *Scientific Reports*, vol. 7, no. 1, p. 39837, Jan 2017.
- [15] H. Lee, H. Park, G. Serhat, H. Sun, and K. J. Kuchenbecker, “Calibrating a Soft ERT-Based Tactile Sensor with a Multiphysics Model and Sim-to-real Transfer Learning,” in *Proceedings of the IEEE International Conference on Robotics and Automation (ICRA)*, 2020, pp. 1632–1638.

[16] Y. Yan, Z. Hu, Z. Yang, W. Yuan, C. Song, J. Pan, and Y. Shen, "Soft magnetic skin for super-resolution tactile sensing with force self-decoupling," *Science Robotics*, vol. 6, no. 51, 2021.

[17] G. Westheimer, "Optical superresolution and visual hyperacuity," *Progress in Retinal and Eye Research*, vol. 31, no. 5, pp. 467–480, 2012.

[18] A. Krause, A. Singh, and C. Guestrin, "Near-Optimal Sensor Placements in Gaussian Processes: Theory, Efficient Algorithms and Empirical Studies," *Journal of Machine Learning Research (JMLR)*, vol. 9, pp. 235–284, February 2008.

[19] N. F. Lepora, U. Martinez-Hernandez, M. Evans, L. Natale, G. Metta, and T. J. Prescott, "Tactile Superresolution and Biomimetic Hyperacuity," *IEEE Transactions on Robotics*, vol. 31, no. 3, pp. 605–618, 2015.

[20] H. Sun and G. Martius, "Robust Affordable 3D Haptic Sensation via Learning Deformation Patterns," in *Proceedings of the IEEE International Conference on Humanoid Robots (Humanoids)*, 2018, pp. 846–853.

[21] H. Sun and G. Martius, "Machine Learning for Haptics: Inferring Multi-Contact Stimulation From Sparse Sensor Configuration," *Frontiers in Neurorobotics*, vol. 13, p. 51, 2019.

[22] Lichuan Liu, S. M. Kuo, and M. Zhou, "Virtual sensing techniques and their applications," in *Proceedings of the IEEE International Conference on Networking, Sensing and Control*, 2009, pp. 31–36.

[23] Ansys®, *Academic Research Mechanical, Release 18.1*, 2020.

[24] P. H. Mott and C. M. Roland, "Limits to Poisson's ratio in isotropic materials – general result for arbitrary deformation," *Physica Scripta*, vol. 87, no. 5, p. 055404, 2013.

[25] P. Dallaire, P. Giguère, D. Émond, and B. Chaib-draa, "Autonomous tactile perception: A combined improved sensing and Bayesian nonparametric approach," *Robotics and Autonomous Systems*, vol. 62, no. 4, pp. 422–435, 2014.

[26] "TakkTile kit." 2021.

[27] L. U. Odhner, L. P. Jentoft, M. R. Claffee, N. Corson, Y. Tenzer, R. R. Ma, M. Buehler, R. Kohout, R. D. Howe, and A. M. Dollar, "A compliant, underactuated hand for robust manipulation," *The International Journal of Robotics Research*, vol. 33, no. 5, pp. 736–752, 2014.

[28] T. Q. Pham, T. Hoshi, Y. Tanaka, and A. Sano, "Effect of 3D microstructure of dermal papillae on SED concentration at a mechanoreceptor location," *PLOS ONE*, vol. 12, no. 12, pp. 1–16, 12 2017.

[29] C. M. Bouthy, M. Negre, M. Jorda, O. Vardoulis, A. Chortos, O. Khatib, and Z. Bao, "A hierarchically patterned, bioinspired e-skin able to detect the direction of applied pressure for robotics," *Science Robotics*, vol. 3, no. 24, 2018.

## APPENDIX A

### APPROXIMATE ANALYTICAL COMPUTATION OF $\sigma_P$

Here we give a closed-form expression relating the force measurement noise to the position accuracy between two taxels, we make a first-order approximation of the intersection area as a parallelogram, as shown in Fig. 9. For two taxels at distance  $D$  and the TVIs described by the following equations

$$I_1^S(d) = g(S) + \lambda|d|^\alpha \quad (9)$$

$$I_2^S(d) = g(S) + \lambda|d - D|^\alpha, \quad (10)$$

we can compute the (absolute) derivatives of the TVIs at the intersection point  $d$ :

$$m_1 := \left| \frac{dI_1^S(d)}{dd} \right| = \lambda\alpha|d|^{\alpha-1} \quad (11)$$

$$m_2 := \left| \frac{dI_2^S(d)}{dd} \right| = \lambda\alpha|d - D|^{\alpha-1}. \quad (12)$$

The trigonometric construction is shown in Fig. 9 and yields the following result:

$$2\sigma_S = a + b = m_1\sigma_P + m_2\sigma_P \quad (13)$$

$$\sigma_P = \frac{2\sigma_S}{m_1 + m_2} \quad (14)$$

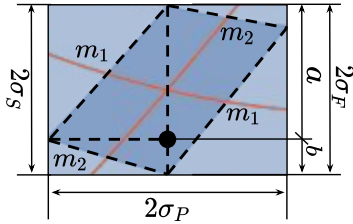


Fig. 9. Intersection area of two TVIs between the taxels can be well approximated by a parallelogram. The slopes of the edges ( $m_1, m_2$ ) are simply given by the inclination of the TVIs at the intersection point (first order approximation).

## APPENDIX B

### PRECISE COMPUTATION OF $\sigma_P$ AND $\sigma_S$

In the above section uses a first-order approximation. In this section, we use the exact corners of the intersection area of the two TVIs with their measurement uncertainty hose. These intersection points are computed numerically and we use this method for all plots in the main paper.

In more detail, we have the following lines defining the TVIs with their uncertainties:

$$h_1^+ = I_1^S(d) + \sigma_S \quad (15)$$

$$h_1^- = I_1^S(d) - \sigma_S \quad (16)$$

$$h_2^+ = I_2^S(d) + \sigma_S \quad (17)$$

$$h_2^- = I_2^S(d) - \sigma_S. \quad (18)$$

There are 4 intersection points:  $h_1^+ \cap h_2^+$ ,  $h_1^+ \cap h_2^-$ ,  $h_1^- \cap h_2^+$ , and  $h_1^- \cap h_2^-$  which we illustrate in Fig. 10. The size of bounding box of these four points defines  $\sigma_P$  and  $\sigma_S$ .

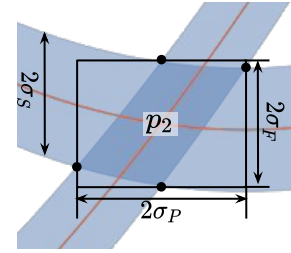


Fig. 10. Computation of  $\sigma_P$  and  $\sigma_S$  based on the intersection types. The  $k$  terms stand for the slopes of the respective lines.

## APPENDIX C

### CURVED SENSING SURFACE

In common applications, the haptic sensor should cover a robot limb or any other curved surface. Figure 11 shows the intersection of TVIs on a cylinder-shaped sensing surface. To extend the TVI analysis from flat 2D to 2.5D (curved 2D surface in 3D), only the distances have to be measured as geodesics on the sensing surface.

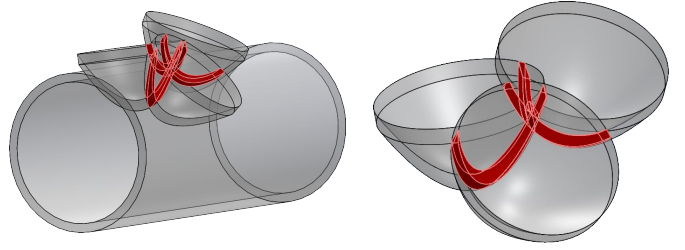


Fig. 11. Intersection of TVIs for the case of a curved sensing surface. The same applies as in the case of planar 2D, except that distances need to be measured as geodesics on the curved surface.

## APPENDIX D

### MORE ON PHYSICAL EFFECTS IN THE FEM MODEL

*Indenter shape:* What is the impact of the indenter shape (or the object getting in touch with the sensing device later) on the TVIs. For illustration, we simulate the displacement caused by three different indenter shapes: a sphere, an ellipsoid, and a cylinder. The displacement decreases and becomes flatter for the cylinder near the contact center as shown in Fig. 12. The cylinder with flatter contact surface causes less sensitivity for shear displacement. As a remark, for too small indenters, there is a risk to exceed the material yield strength and break the contact surface material.

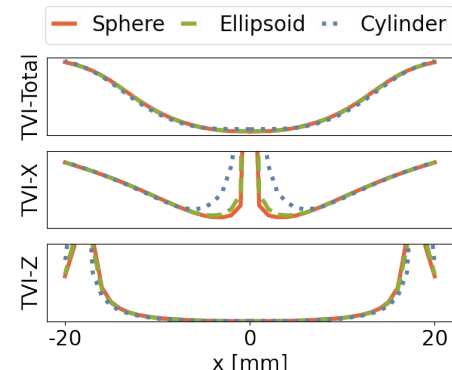


Fig. 12. TVIs analysis for different indenter shapes.

## APPENDIX E

## DETAILS OF THE REAL SINGLE TAXELS EVALUATION

Here we provide more details for Section 6.

**TVIs:** : We implement the following steps to compute the isolines: first, we linearly interpolate the sensor values and force values; second, we choose a position-related sensor value and find the corresponding force measurement in that position; third, we draw the position-force curve for that sensor value with the same color.

**Experimental Details:** : The strain gauge sensor is EP08-250AE-350, the accelerometer is ADXL345, and the barometer is MPL3115A2. We solder extra thin wires to the chips to be able to mold them inside the elastomer with minimal mechanical influence of the taxel. We mold these three sensors floating in the middle and center of three elastomer pieces (EcoFlex 00-30) individually, each with a diameter of 120 mm and a thickness of 10 mm. Additionally, we build a 3-DoF test bed (Barch Motion) equipped with a 3-axis force measurement device (ATI Mini40) to indent the elastomer surface in a precise and automated way. As shown in Fig. 7(A), a 4 mm spherical indentor goes along two black-colored perpendicular trajectories where each sensor unit is located under the cross point. The test bed is used to make the indentor contact 100 positions evenly spread along each trajectory (from -50 mm to 50 mm) with 25 incremental indentation depths (0.2 mm each) at each position. The sensor value of the strain gauge (EP08-250AE-350) is acquired through a quarter Wheatstone bridge and amplified in the MCP609; the sensor values of the

accelerometer (ADXL345) and the barometer (MPL3115A2) are acquired through the evaluation boards supplied by the Adafruit; and all of them are delivered to a laptop (ThinkPad L570) through Arduino Mega 2560. The recorded data are sensor values, force values, and indentation positions and depths. For different indentation depths, the sensor values vary along the indentation positions, and deeper indentations need higher forces and result in higher sensor values. When the indentation positions are near the placed sensor units, the applied forces are higher because the physical sensor unit is stiffer than the elastomer.

APPENDIX F  
MULTI-BARODOM SENSOR DETAILS

A remark on the stronger noise level in the force prediction as shown in Fig. 8. When collecting the data, the test bed did not pause sufficiently but continued to measure values quicker than a stationary situation was reached.

## F.1. Machine Learning Model

We use a standard MLP (multi-layer-perceptron) with six fully connected hidden layers with 50 neurons each. The data consist of 40 k samples that are split into datasets of training, validation, and test with a ratio of 3:1:1. The models are trained with the L2 loss and a batch size of 500 samples in 100 k iterations. The results are evaluated on the test set that was not used otherwise.